

Carbon Geological Storage: Coupled Processes, Engineering and Monitoring

Seunghee Kim¹, D. Nicolas Espinoza², Jongwon Jung³,
Minsu Cha⁴ and J. Carlos Santamarina⁵

¹Department of Civil Engineering, University of Nebraska-Lincoln, Lincoln, NE, United States

²Department of Petroleum and Geosystems Engineering, The University of Texas at Austin, Austin, TX, United States ³School of Civil Engineering, Chungbuk National University, Cheongju, South Korea

⁴Zachry Department of Civil Engineering, Texas A&M University, College Station, TX, United States

⁵Earth Science and Engineering, King Abdullah University of Science and Technology, Thuwal, Saudi Arabia

INTRODUCTION

Fossil fuels (petroleum, coal, and natural gas) account for about 85% of the primary energy consumed worldwide. All predictors suggest a decreased share of fossil fuels in the total energy mix (from 85% to about 79%), yet the absolute consumption of fossil fuels will increase by another 36% in the next 25 years.

Fossil fuel reserves exceed several generations at current rates of consumption. However, there is an increasing concern with rising CO₂ levels in the atmosphere and its implications on climate change. The United States emits 6.8 billion tons of CO₂ every year—enough to fill a 10-m deep pool with the size of New York City—780 km²—with liquid CO₂. The annual worldwide CO₂ emission is six times higher. Based on present trends, the energy challenge and the environmental consequences of CO₂ will reach a critical point within the next 20–30 years. The cost of carbon capture and storage will range between 1% and 2% of the gross domestic product (for reference, the worldwide military expenditure is ~2.1% of the gross world product).

The energy challenge is not about reserves, at least not in the short term, it is about the large anticipated increase in demand within the next generation, the current dependency on fossil fuels and climate implications, and the geographic mismatch between resources and demand.

The situation is aggravated by the disparity in timescales for phenomena that affect national decisions (e.g., the 4-year political cycle), to timescales for phenomena that affect energy infrastructure and the environment (e.g., 50-year design life for energy infrastructure and the 100,000 year half-life of some radioactive isotopes in high-level nuclear waste).

The long-term geological storage of vast quantities of CO₂ is a relatively new scientific and technological challenge. This manuscript explores underlying coupled hydro-chemo-mechanical processes, potential emergent phenomena, and implications to monitoring. Salient properties such as density, interfacial tension, and capillary forces are reviewed first, followed by the analysis of coupled hydro-chemo-mechanical processes, including acidification, mineral dissolution, and mechanical implications. These foundations guide the analysis of CO₂ storage in saline aquifers, coal seams, depleted reservoirs, and in the form of hydrates. The chapter ends with a review of monitoring and leakage-sealing strategies and the identification of the most important dimensionless ratios that govern CO₂ geo-storage.

MIXED FLUID PHENOMENA

Density

The physical properties of CO₂ depend on pressure–temperature PT conditions. CO₂ is a gas at normal temperature and pressure, it changes into a liquid state at moderate pressures ~6.4 MPa at 298 K, and becomes supercritical when the temperature is higher than 304.1 K and the pressure is greater than 7.38 MPa (Fig. 17.1). At typical reservoir PT conditions:

- CO₂ is less dense than brine, hence, buoyant forces develop in CO₂–brine multiphase systems. Fig. 17.2 shows typical pressure and temperature profiles onshore and offshore, and the corresponding variation in CO₂ density estimated using an equation of state (Peng and Robinson, 1976; Span and Wagner, 1996).
- CO₂ is five to >10 times less viscous than water, as shown in the viscosity versus depth trend for onshore and offshore conditions in Fig. 17.2 (for example: $\mu_{CO_2} \sim 50 \times 10^{-6}$ Pa·s at 20 MPa and 360 K; Fenghour et al., 1998).

Water–CO₂–Mineral Interaction: Interfacial Tension and Contact Angle

The wettability of reservoir rocks and minerals controls CO₂ invasion and lateral spread, residual water saturation, caprock breakthrough pressures, and leakage. The Young–Laplace equation prescribes the capillary entry pressure $P_c = P_{CO_2} - P_w$ of CO₂ into originally water-filled pores as a function of the CO₂–water interfacial tension σ_{fl} , the contact angle θ formed by the water–CO₂ interface on the mineral surface, and the minimum pore size d along a percolating path across the medium (Espinoza and Santamarina, 2012):

$$P_c = \frac{\psi \sigma_{fl} \cos\theta}{d} \quad (17.1)$$

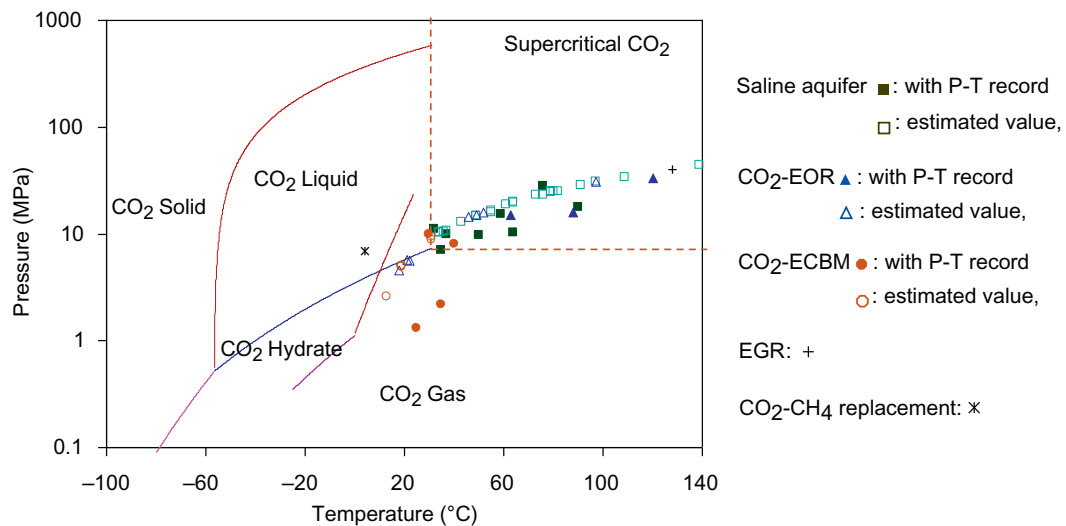


FIGURE 17.1 CO₂ Phase diagram. Pilot CO₂ injection projects are superimposed on this plot. Unless reported in the original sources, the PT conditions are estimated as: $P = \gamma_w z$, $T = T_0 (4^\circ\text{C}) + 30^\circ\text{C}/\text{km} \times z$ (CO₂ hydrate phase boundary from: Sloan and Koh, 2007; Takenouchi and Kennedy, 1965). Source: Modified from Espinoza, D.N., Kim, S., Santamarina, J.C., 2011. CO₂ geological storage—geotechnical implications. KSCE J. Civil Eng. 15, 707–719.

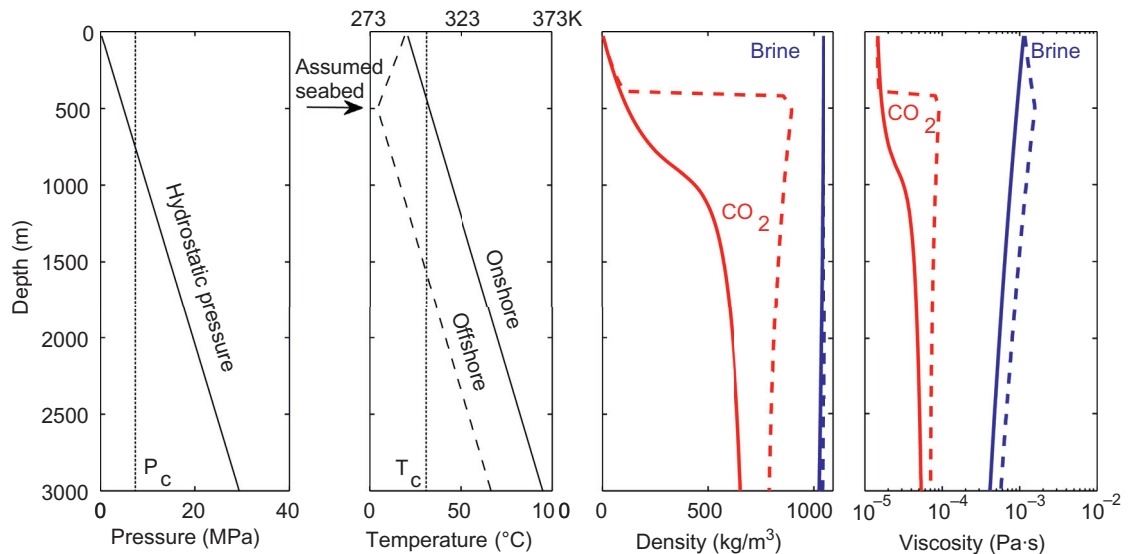


FIGURE 17.2 Mass density and dynamic viscosity of CO₂ and brine as a function of depth and corresponding PT conditions. CO₂ is lighter and less viscous than water and brine. Source: Modified from Espinoza, D.N., Kim, S., Santamarina, J.C., 2011. CO₂ geological storage—geotechnical implications. KSCE J. Civil Eng. 15, 707–719.

where the ψ -factor reflects the pore shape ($\psi=4$ for cylindrical tubes and $\psi=2$ for parallel plates). Experimental data indicates that breakthrough in homogeneous media happens along pores which are larger than the mean pore size, $d > d_{mean}$ (Espinoza and Santamarina, 2010).

The CO_2 –water interfacial tension is pressure dependent, and it follows a quasi-linear inverse relationship with the PT-dependent mass density of CO_2 , from 72 mN/m for CO_2 gas at standard pressure and temperature, to ~ 30 mN/m for liquid CO_2 , and it remains almost constant thereafter (Chalbaud et al., 2009).

Wettability, i.e. contact angle θ , is more variable and difficult to predict. The contact angle formed by the CO_2 –water interface on mineral surfaces varies for different minerals: $\theta \sim 85^\circ\text{--}95^\circ$ on oil-wet amorphous silica, $\theta \sim 50^\circ\text{--}120^\circ$ on coal, $\theta \sim 40^\circ\text{--}60^\circ$ on mica, $\theta \sim 40^\circ$ on water-wet amorphous silica and calcite surfaces, and $\theta \sim 8^\circ\text{--}30^\circ$ on organic shale surfaces (note: angle measured through the water phase in all cases (Guiltinan et al., 2017; Espinoza and Santamarina, 2010; Chalbaud et al., 2009; Chi et al., 1988)).

The Young-Dupré equation relates the contact angle θ to the interfacial tensions σ : $\cos\theta = (\sigma_{fs} - \sigma_{ls}) / \sigma_{fl}$, (Rotenberg et al., 1983; Fig. 17.3). Therefore, the contact angle in water– CO_2 –mineral systems is affected by changes in interfacial tensions σ_{fs} , σ_{ls} , and σ_{fl} with pressure, temperature, and salinity: average net increase in the contact angle on a silica surface is $18^\circ \pm 2^\circ$ with an increase of pressure from 0.1 MPa to 25 MPa, and average net increase is $20^\circ \pm 2^\circ$ for an increase in ionic strength from 0 M to 5 M (Jung and Wan, 2012).

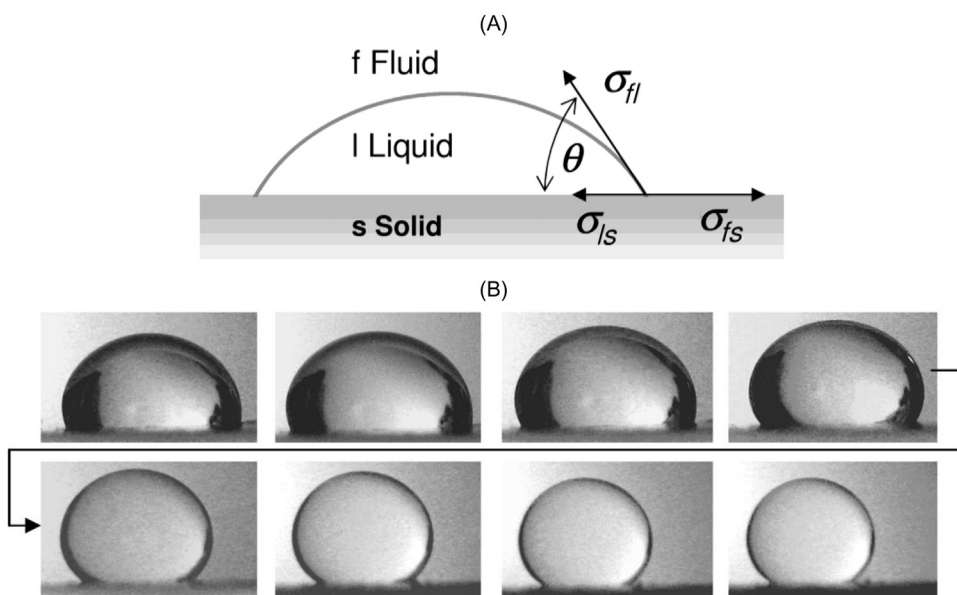


FIGURE 17.3 Interfacial tensions σ and contact angle θ . (A) Definitions: surrounding fluid f , fluid droplet l and solid substrate s . (B) Changes in the interfacial tension σ and contact angle θ with increasing pressure from 0.1 to 18.5 MPa—water droplet surrounded by CO_2 on CO_2 -wet substrate. Source: Modified from Espinoza, D.N., Santamarina, J.C., 2010. Water- CO_2 -mineral systems: interfacial tension, contact angle, and diffusion—implications to CO_2 geological storage. *Water Resour. Res.* 46, W07537.

Buoyancy and Capillarity: CO₂ Plume Thickness

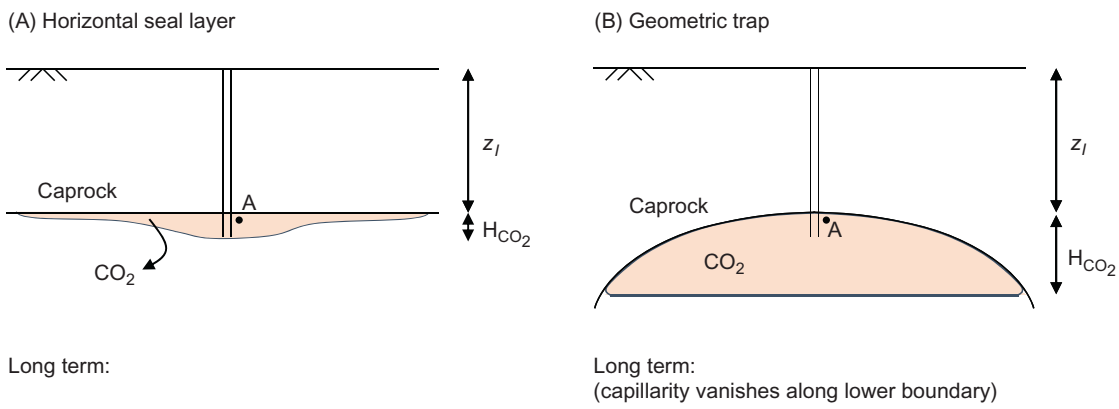
The balance between the overpressure generated by the buoyant CO₂ plume ($\gamma_B - \gamma_{CO_2}$) H_{CO_2} , and the capillary entry pressure P_c required to invade the storage reservoir (Young–Laplace equation) determine the quasi-static lateral spread of the CO₂ plume in the absence of structural or stratigraphic features. Therefore, the CO₂ plume thickness H_{CO_2} (m) is a function of the interfacial tension between the CO₂ and brine, σ_{fl} (mN/m), the characteristic pore diameter in the storage reservoir, d_{ch} [m], and the unit weights of CO₂ and brine, γ_{CO_2} and γ_B :

$$H_{CO_2} \leq \frac{4\sigma_{fl}}{d_{ch}(\gamma_B - \gamma_{CO_2})} \quad (17.2)$$

For example, the plume thickness is $H_{CO_2} = 3$ m in a reservoir with characteristic pore size $d_{ch} = 10 \mu\text{m}$ (assumed: $\sigma_{fl} = 30 \text{ mN/m}$ and $\gamma_B - \gamma_{CO_2} = 4 \text{ kN/m}^3$ for $P = 10 \text{ MPa}$ and $T = 40^\circ\text{C}$).

Clearly, there is a tradeoff between injectivity (facilitated in larger pore size reservoirs) and capillary trapping and CO₂ pool thickness (more effective in smaller-pore-size reservoirs). We can anticipate that the thickness of CO₂ plumes in flat layered sediments will be typically thinner than $H_{CO_2} < 10$ m, and impose small overpressures typically $<40 \text{ kPa}$ (see also Bielinski, 2007; Hesse et al., 2006; Pruess, 2011).

The excess pressure required during CO₂ injection will gradually vanish after injection stops. The asymptotic long-term CO₂ pressure within the reservoir results from buoyancy and capillary entry pressure at the plume boundaries. Fig. 17.4 illustrates long-term CO₂ pressures for horizontal caprocks and geometric traps.



$$@A: P_{CO_2} = \gamma_B z_l + \frac{4\sigma_{fl}}{d_{ch}}$$

$$@A: P_{CO_2} = \gamma_B z_l + H_{CO_2} (\gamma_B - \gamma_{CO_2})$$

FIGURE 17.4 CO₂ pressure P_{CO_2} . (A) Horizontal caprock upper boundary. (B) Geometric trap. Note: depth to caprock-storage reservoir boundary z_l (m), CO₂ plume thickness H_{CO_2} (m), CO₂ pressure P_{CO_2} (Pa), brine γ_B and CO₂ γ_{CO_2} unit weights (N/m³), interfacial tension between CO₂ and brine σ_{fl} (N/m), and characteristic pore size in the storage reservoir: d_{ch} (m). Source: Modified from Kim, S., Santamarina, J.C., 2014. CO₂ geological storage: hydro-chemo-mechanical analyses and implications. *Greenh. Gas. Sci. Technol.* 4, 528–543.

Interparticle Capillary Forces

Fine-grained seal layers are sensitive to capillary forces (i.e. suction s), and can experience swelling during wetting or volumetric contraction and even desiccation cracks during drying (Espinoza and Santamarina, 2012; Sánchez et al., 2005; Shin and Santamarina, 2011). An increase in the suction Δs leads to a decrease in the void ratio $\Delta e = -(\kappa_s/s)\Delta s$, proportional to the sediment compressibility κ_s (Alonso et al., 1990). High specific surface area in clays such as montmorillonite is more prone to volumetric contraction.

CHEMO-HYDRO-MECHANICAL PHENOMENA

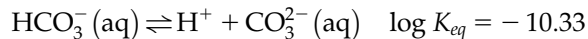
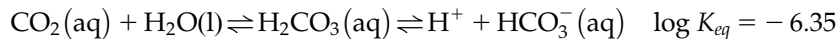
Water–CO₂ Solubility, Acidification, and Diffusivity

CO₂ dissolves in water to form aqueous carbon dioxide CO₂(aq). The solubility of CO₂ in water x_{CO_2} (mol/L) can be estimated using Henry's law (Espinoza et al., 2011):

$$x_{\text{CO}_2} = k_H \varphi_{fu} P_{\text{CO}_2} \quad (17.3)$$

where the Henry's coefficient is $k_H \approx 10^{-1.46} = 0.0347$, and the fugacity coefficient $\varphi_{fu} \leq 1$ can be estimated using an equation of state. Water at room temperature and at 0.1 MPa contains $x_{\text{CO}_2} \approx 0.03\text{--}0.04$ mol/L. The solubility of CO₂ in water increases by two orders of magnitude $x_{\text{CO}_2} \approx 1\text{--}2$ mol/L at reservoir PT conditions, and it can reach 1–2 moles of CO₂ per liter of brine. On the other hand, water dissolves into CO₂ as well; for example, ~ 0.05 mole of water dissolves per kg of CO₂ at 10 MPa and 285 K (Spycher et al., 2003).

Aqueous carbon dioxide mixes with the water to produce carbonic acid and ionizes in a step-wise progression:



The final result is ion bicarbonates, an increase in H⁺, and a decrease in pH. At reservoir PT conditions acidity can reach pH ≈ 3 .

The diffusivity of water into liquid CO₂ is high and can reach $D \approx 2\text{--}20 \times 10^{-8}$ m²/s at 7–25 MPa and 305 ± 10 K (Espinoza and Santamarina, 2010). On the other hand, the diffusivity of supercritical CO₂-in-water is $D \approx 2 \times 10^{-8}$ m²/s at 313 K (Funazukuri et al., 1992; Liong et al., 1992).

Changes in Interparticle Electrical Forces

Caprocks and seal layers react to changes in the pore fluid chemistry. In particular, the surface charge of clay minerals is pH-dependent: low pH promotes protonation, leading to positively charged surfaces (Lyklema, 1995; Santamarina et al., 2001; Stumm, 1992). Hydrated ions

are attracted to charged clay surfaces, form a diffuse counterion cloud, and give rise to electrostatic repulsion among contiguous particles. In addition, CO₂ is a nonpolar, low-permittivity fluid. Hence, a change in electrical interparticle forces is expected as CO₂ fills the pore space. The implications include a reduction in the osmotic repulsion and a three fold increase in the Hamaker constant for clay–CO₂–clay compared to clay–water–clay (Espinoza and Santamarina, 2012).

Mineral Dissolution and Precipitation

The dissolution reaction equilibrium constant denotes the concentration of produced species relative to the concentration of reactant species at steady state conditions, i.e. a function of mineral solubility (note: representative chemical reactions and typical reaction rates are summarized in Espinoza et al., 2011). The solubility of minerals in water depends on pH (Stumm and Morgan, 1996), temperature, pressure (i.e. CO₂ solubility and pH), and concentration of other species (Fredd and Fogler, 1998a; Pokrovsky et al., 2005).

For example, consider a 1-mm spherical grain made of calcite, anorthite, and kaolinite submerged into water acidified by 1 mole of dissolved CO₂ per liter (pH~3). Silicates yield more dissolved cations (pH up to 8) than carbonates (pH up to 5) but the reaction rate is much slower (Gunter et al., 2000). In fact, the time required to dissolve the 1-mm grains is 4 hours for calcite, 16 years for anorthite, and 226 years for kaolinite (based on dissolution rates in Espinoza et al., 2011 and assuming that the system is far from equilibrium).

An idealized CO₂ storage reservoir can be analyzed into four different concentric zones around the CO₂ injection well according to the prevalent chemical reactions (Fig. 17.5; Kim and Santamarina, 2014a). The far-field Zone I is not affected by CO₂ injection and brine saturation remains at $S_B = 1$. Acidified brine dominates Zone II and mineral dissolution prevails over precipitation; loaded with dissolved CO₂ and minerals, denser brine experiences convection, and sustains further dissolution (Hassanzadeh et al., 2007; Riaz et al., 2006). Brine acidification by CO₂ dissolution, water dissolution into CO₂, mineral dissolution, and salt precipitation coexist in the transitional Zone III. The continuous influx of “dry” CO₂ in Zone IV around the injection well, displaces brine first and then dries the residual brine; salt precipitates and CO₂ saturation approaches $S_{CO_2} \approx 1$.

Permeability Changes

Changes in interparticle forces and compaction, salt precipitation, and mineral dissolution change the porosity and pore connectivity, and alter the permeability (Phillips, 2009).

- 1. Compaction.** The Kozeny–Carman type equation (Carman, 1956) anticipates a power-law relationship between normalized porosity φ/φ_o and normalized permeability k/k_o for porous/granular media during compaction: $k/k_o = (\varphi/\varphi_o)^\alpha$ where k_o is the permeability at a known porosity φ_o (Ren and Santamarina, 2018). The exponent ranges between $\alpha = 3$ and 6 for sediment compaction (Mohamed and Nasr-El-Din, 2012; Wellman et al., 2003).
- 2. Precipitation.** Consider a pore network filled with brine. Nonwetting CO₂ invades at a constant flow rate until it percolates the pore network (algorithm described in Kim, 2012). Network simulation results show a quasi-linear trend between the decrease in CO₂

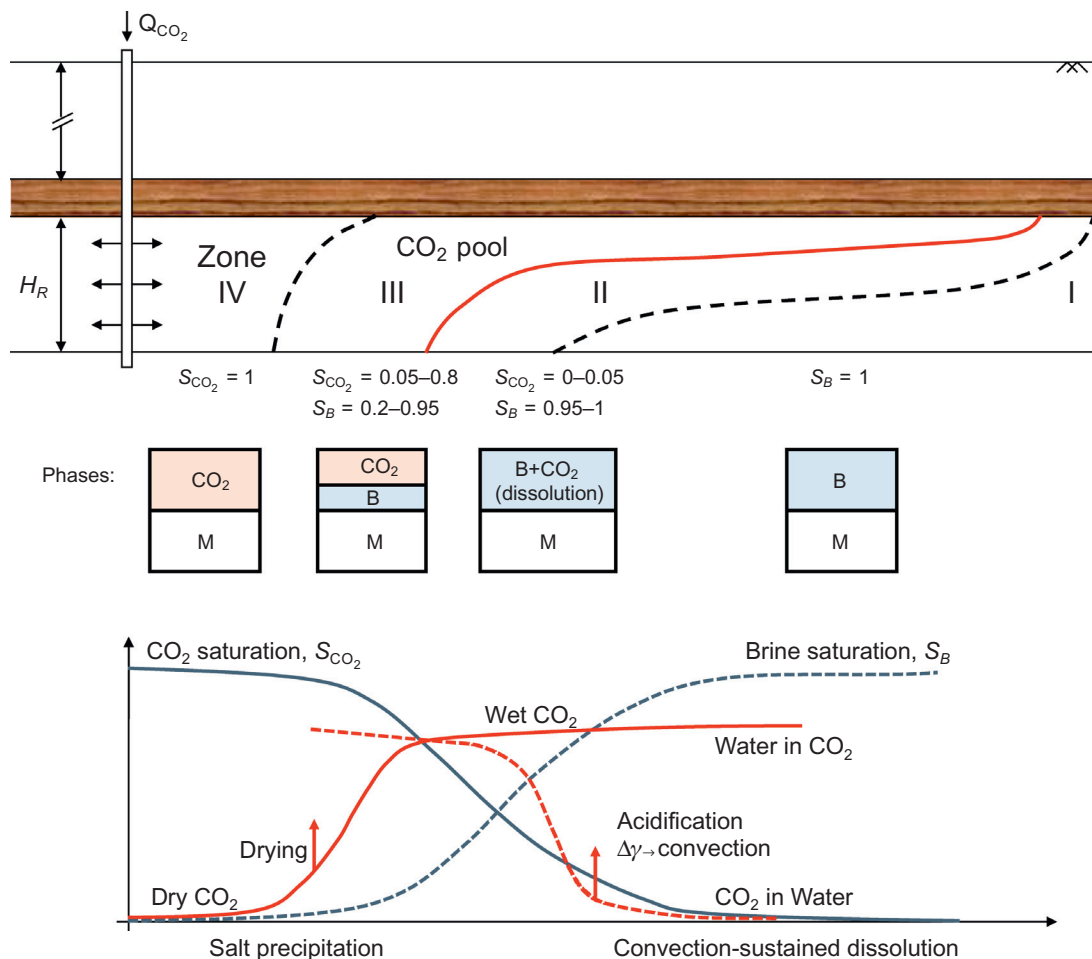


FIGURE 17.5 Zones around a CO₂ injection well (see also Azaroual et al., 2007): from the far-field: Zone I ($S_B = 1$), Zone II ($0.95 \leq S_B \leq 1$), Zone III ($0.2 \leq S_B \leq 0.95$), and Zone IV ($S_{CO_2} \approx 1, S_B \approx 0$). Symbols: M, Mineral; B, Brine; and CO₂ Saturation: S_{CO_2} for CO₂ saturation, and S_B for brine. Source: Modified from Kim, S., Santamarina, J.C., 2014a. CO₂ geological storage: hydro-chemo-mechanical analyses and implications. *Greenh. Gas. Sci. Technol.* 4, 528–543.

permeability and the residual brine saturation S_B (Kim and Santamarina, 2014a). The theoretical-maximum decrease in CO₂ permeability in a capillary tube bundle model is ~35% when the available dissolved salt precipitates in the tubes. However, when precipitation is limited to brine at its residual saturation $0.3 < S_B < 0.5$, the decrease in CO₂ permeability is <20% as the invasion of CO₂ and brine displacement take place along the largest interconnected pores. While the decrease in permeability is relatively small for continuous injection, intermittent injection will cause cyclic brine invasion back into Zone I; cyclic invasion and drying may cause gradual salt accumulation and an additional decrease in permeability (Miri and Hellevang, 2016; Peysson et al., 2014).

3. Dissolution. Dissolution may experience positive feedback:

seepage → dissolution → porosity → seepage, and lead to localization and channeled flow. The timescales for advection t_{adv} and diffusion t_{diff} within a characteristic length L_{ch} , and the chemical reaction time t_{rtn} can be combined to form two dimensionless ratios:

$$\text{Damköhler number } Da = \frac{t_{adv}}{t_{rtn}} = \frac{\kappa L_{ch}}{v_{ave}} \quad (17.5)$$

$$\text{Peclet number } Pe = \frac{t_{diff}}{t_{adv}} = \frac{v_{ave} L_{ch}}{D} \quad (17.6)$$

where κ is the reaction rate (s^{-1}), v_{ave} (m/s) is the average pore velocity, and D (m^2/s) is the molecular diffusion coefficient.

The plot in Fig. 17.6 summarizes observed dissolution patterns as functions of the Damköhler number Da (Fredd and Fogler, 1998b; Golfier et al., 2002). Water with dissolved CO_2 travels through a carbonate system and causes compact nonlocalized dissolution in the far field, but it localizes into a few enlarged flow channels near the inlet.

The coefficient of variation in pore size COV is larger in fractured rock masses than in sediments (Phadnis and Santamarina, 2011; Wellman et al., 2009). Pore network simulations show that media with higher pore size variability COV will experience higher flow localization and fewer channels will carry most of the flow (Fig. 17.7; Kim and Santamarina, 2015); thus, pore size variability exacerbates the consequences of mineral dissolution and flow channeling. Proper upscaling is required to capture localization effects at the continuum-scale.

Stress Changes—Mechanical Implications

Mineral dissolution within the reservoir (Zones II and III) can lead to changes in effective stress, shear failure, compaction, and potential “undermining” of the caprock. These consequences are explored next.

1. *Decrease in K_o with dissolution.* Experimental and numerical results show that the grain dissolution at zero lateral strain affects the ratio $K_o = \sigma_h'/\sigma_v'$ between the horizontal σ_h' and the vertical effective stresses σ_v' (Cha and Santamarina, 2014; Shin and Santamarina, 2009).

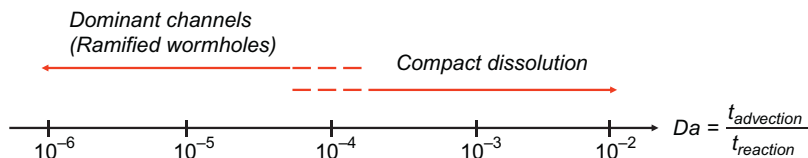


FIGURE 17.6 Dissolution patterns observed as a function of the Damköhler number Da . Note: results obtained using pore-network simulations ($Da = 1.5 \times 10^{-3}$ to $Da = 1.5 \times 10^{-5}$) after 1000 flushed pore volumes of CO_2 -dissolved water. Source: Modified from Kim, S., Santamarina, J.C., 2015. Reactive fluid flow in CO_2 storage reservoirs: a 2-D pore network model study. Greenh. Gas. Sci. Technol. 5, 462–473.

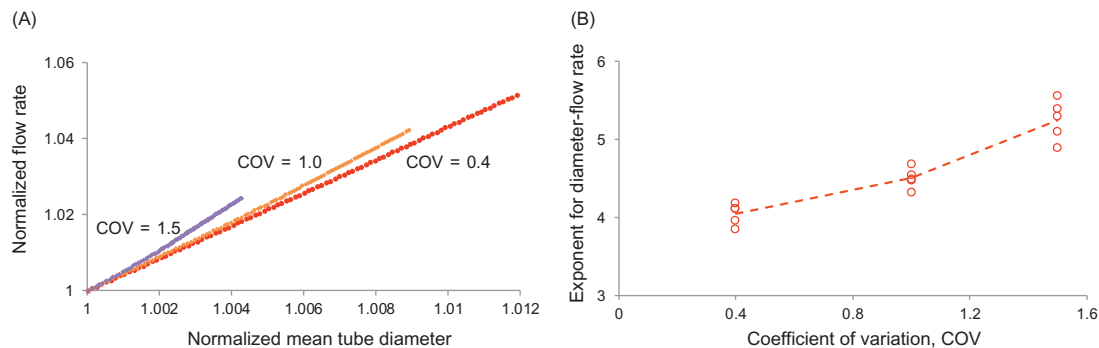


FIGURE 17.7 Mineral dissolution: Flow rate versus mean tube diameter evolution for different pore-size variability—in terms of coefficient of variations COV in tube diameters. (A) Trends during the first 1000 flushed pore volumes (at $Da \sim 1 \times 10^{-5}$), and (B) exponent α that relates normalized flow rate-normalized diameter change, $(q/q_0) = (\bar{d}/\bar{d}_0)^{\alpha}$, for different pore-size variability. Source: Modified from Kim, S., Santamarina, J.C., 2015. Reactive fluid flow in CO_2 storage reservoirs: a 2-D pore network model study. *Greenh. Gas. Sci. Technol.* 5, 462–473.

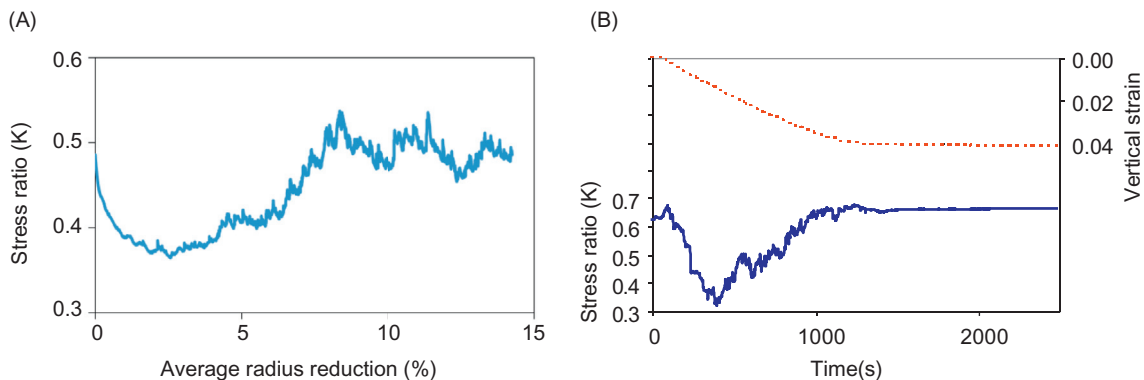


FIGURE 17.8 Evolution of lateral stress coefficient K during dissolution. (A) Pressure solution—2-D DEM simulation (Source: Modified from Cha, M., Santamarina, J.C., 2014. Dissolution of randomly distributed soluble grains: post-dissolution k_0 -loading and shear. *Géotechnique* 64, 828–836), and (B) laboratory tests: 10% salt (Source: Modified from Shin, H., Santamarina, J.C., 2009. Mineral dissolution and the evolution of k_0 . *J. Geotech. Geoenviron. Eng.* 135, 1141–1147).

Grain mass loss due to mineral dissolution can produce a pronounced horizontal stress drop under zero lateral strain conditions (Fig. 17.8), and the state of stress may reach the Coulomb failure envelope. Lateral displacement becomes negligible when the affected layer thickness is much smaller than the plume lateral extent. In the absence of re-precipitation, sediments are more compressible after dissolution; the increase in compressibility correlates with the extent of dissolution.

2. *Formation of shear bands during dissolution.* Studies of grain dissolution using discrete element numerical simulations show the spontaneous formation of shear bands and displacement localization when dissolution is proportional to interparticle forces. Fig. 17.9 presents snapshots of contact force chains and strain fields during pressure solution. There are

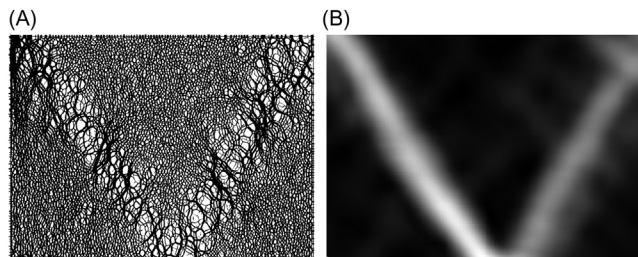


FIGURE 17.9 Localized deformation and shear bands as a consequence of grain size reduction (normal-force dependent) to mimic pressure solution (2-D DEM simulation). (A) Contact force chains, and (B) strain field. (Note: strain field computed as the gradient of accumulated displacements from the beginning of dissolution). *Source: Modified from Cha, M., 2012. Mineral Dissolution in Sediments. Georgia Institute of Technology, Atlanta, USA.*

marked force chains inside the shear bands at a characteristic angle of $\sim 50^\circ$ – 60° with the shear band. These strong force chains form and buckle as force-dependent dissolution progresses. Dissolution is faster in the shear bands than in the wedges. The emergence of shear discontinuities during pressure solution under zero lateral strains may explain the nontectonic origin of shear discontinuities and polygonal fault systems observed in marine sediments and lacustrine deposits (Cartwright et al., 2003; Shin et al., 2008, 2010). By analogy, CO₂-driven mineral dissolution may lead to the formation of similar discontinuities in a storage reservoir under zero lateral strains.

3. *Bending Failures.* Dissolution within CO₂ geo-storage reservoirs could undermine the caprock in Zones II and III. Under the weight of the overburden, the seal layer will follow the reservoir and may eventually experience bending and/or shear failure. Clearly, potential seal layers must be continuous and ductile to deform without developing high-permeability pathways (De Paola et al., 2009; Downey, 1984).

Note that this section itself is focused on stress changes due to mineral dissolution, rather than thermally and/or hydraulically induced stress change during the injection of nonisothermal CO₂.

STORAGE: TRAPPING MECHANISMS

Natural accumulations of CO₂ in the Earth's upper crust range from CO₂ pools (e.g., Ladbroke Grove and Katnook Gas Fields in southeastern Australia; Watson et al., 2004) to the massive carbonate deposits worldwide (i.e. sun-fueled, biogenic CO₂ capture and storage). Clearly, we can count on physical, biological, and chemical trapping mechanisms to keep CO₂ within geological formations (Dooley et al., 2006; IPCC et al., 2005; Jaccard, 2005). Physical trapping mechanisms include structural and stratigraphic trapping beneath seal layers or caprocks, hydrodynamic trapping by slow aquifer currents, and capillary trapping. Chemical trapping mechanisms involve the dissolution of CO₂ in water, mineralization, CO₂ adsorption on coal and rich-organic shales (includes the use of CO₂ in enhanced oil recovery), and CO₂ hydrate formation.

Stratigraphic Traps

The caprock acts as a structural trap and resists the short-term excess injection pressures, and the long-term pressure gradient caused by the buoyant CO_2 (Fig. 17.10). As noted earlier, the buoyant supercritical CO_2 creates modest static overpressures in flat accumulations, and it can reach 0.27–0.4 MPa for a 100-m interconnected column of CO_2 .

The measured CO_2 breakthrough pressures are less than ~6.2 MPa in mudrocks and less than ~11.2 MPa in evaporite rocks (Espinoza and Santamarina, 2017). These breakthrough measurements suggest that percolating paths connect pores larger than >15 nm in mudrocks and >9 nm in evaporites.

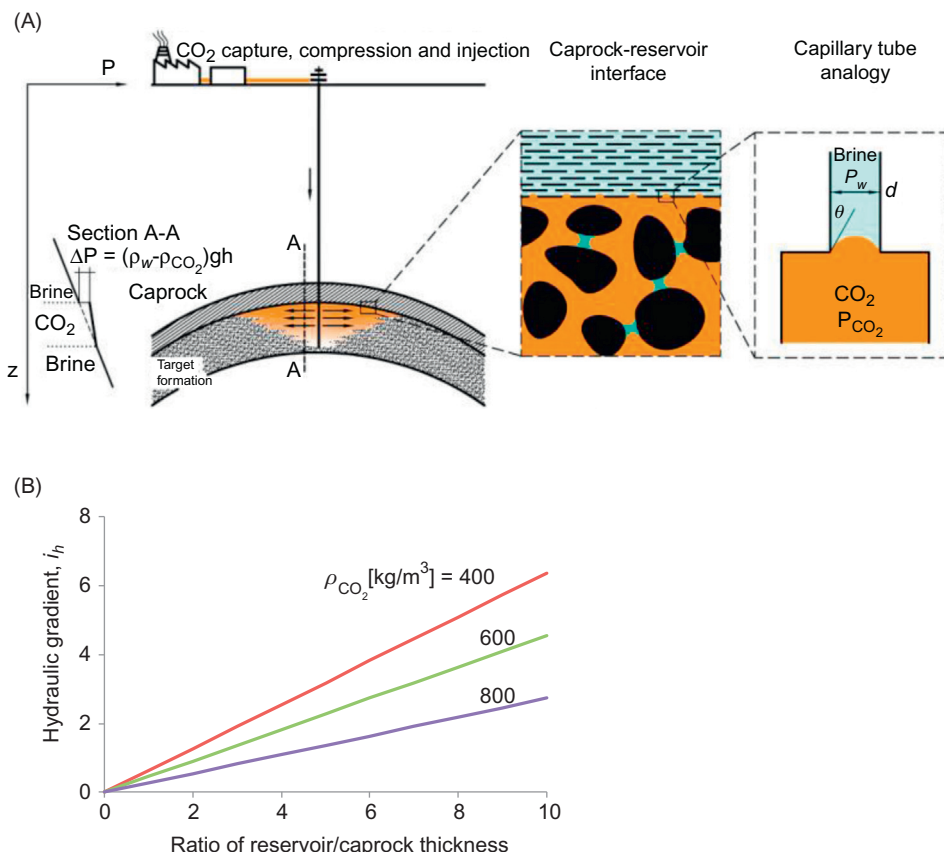


FIGURE 17.10 Caprock sealing. (A) The pressure difference across the caprock caused by the buoyant CO_2 is resisted by CO_2 -water capillary menisci. Viscous forces oppose CO_2 buoyancy after breakthrough. (B) Hydraulic gradient i_h for the upward flow through the caprock with different CO_2 densities. Source: Modified from Kim, S., 2012. CO_2 Geological Storage: Hydro-Chemo-Mechanically Coupled Phenomena and Engineered Injection. Georgia Institute of Technology, Atlanta, GA, USA; and Espinoza, D.N., Santamarina, J.C., 2017. CO_2 breakthrough—caprock sealing efficiency and integrity for carbon geological storage. Int. J. Greenh. Gas Control 66, 218–229.

Pathways filled with percolating CO₂ phase and the caprock permeability determine post-breakthrough CO₂ transport (Fleury et al., 2010; Gherardi et al., 2007). The low viscosity of CO₂ and the low water–CO₂ interfacial tension enhance the risk of leakage. Let us consider an overpressure $\Delta P = H_{\text{CO}_2}(\gamma_w - \gamma_{\text{CO}_2})$ caused by a CO₂ plume of thickness H_{CO_2} . The gradient i_h across the caprock of thickness H_c (m) takes into consideration differences in elevation and pressure in terms of the total head Δh_T :

$$i_h = \frac{\Delta h_T}{H_c} = \left(\frac{H_{\text{CO}_2}}{H_c} \right) \cdot \left(1 - \frac{\gamma_{\text{CO}_2}}{\gamma_w} \right) \quad (17.7)$$

The estimated hydraulic gradient for most sites currently under consideration is quite small and would rarely exceed $i_h < 10$ (Fig. 17.10). The permeability K_{con} (cm/s) for typical seal rocks ranges between 10^{-10} cm/s and 10^{-13} cm/s in the absence of discontinuities. Then, estimated transport velocities $v = k \cdot i_h$ are very low and will remain lower than 10^{-4} – 10^{-8} m/year.

The seal layer efficiency can be summarized in terms of two dimensionless ratios to evaluate trapping and transport conditions:

- *Peclet number*: $10^{-6} < Pe < 10^{-3}$ for the anticipated hydraulic gradients $i_h < 10$ (a ratio of cross-layer advective flow to cross-layer diffusion). Therefore, diffusion-controlled reactive transport prevails over advective transport in the caprock.
- *Sealing number Sl* (ratio between the capillary entry pressure and the overpressure at the caprock–reservoir interface): For a pore sized <0.1 μm (most seal rocks without discontinuities), and an anticipated CO₂ column height $H_{\text{CO}_2} \leq 100$ m, the sealing number is $Sl > 4$, and CO₂ containment is anticipated. The same dimensionless ratio applies to lateral capillary trapping.

Coal and Shale: CO₂ Adsorption and CH₄ Desorption

The fabric of organic-rich phases in coal and shale consists of a microporous disordered organic frame. These small pores ($d \sim 10^{-9}$ – 10^{-8} m) allow the adsorption and desorption of gases, including CO₂, CH₄, and N₂. The high specific internal surface of the microporous structure can retain 1–10 m³/m³ of adsorbed gases. Thus, coal seams and organic-rich shales are potential sources of CH₄ and sinks for CO₂ (Busch et al., 2008; Kang et al., 2011).

Fluid transport through coal and shale combines diffusion and slow advection (Ceglarska-Stefańska and Zarebska, 2002). In fact, global flow is dominated by high-permeability pathways such as fractures (Espinoza et al., 2016).

Volumetric strains ε_v are associated with adsorption, desorption, and gas replacement, and can range from $\varepsilon_v \sim 10^{-3}$ in shale to $\varepsilon_v > 10^{-2}$ in coal—Fig. 17.11 (Chen et al., 2015; Shovkun and Espinoza, 2017). The associated changes in permeability can exceed two orders of magnitude (Pan and Connell, 2012): (1) permeability increases during primary methane production due to desorption-induced shrinkage, cleat opening, shear fracturing, and dilation (Espinoza et al., 2015; Palmer and Mansoori, 1996; Scott et al., 2012); (2) conversely, permeability decreases during CO₂ injection due to adsorption-induced swelling and cleat closing.

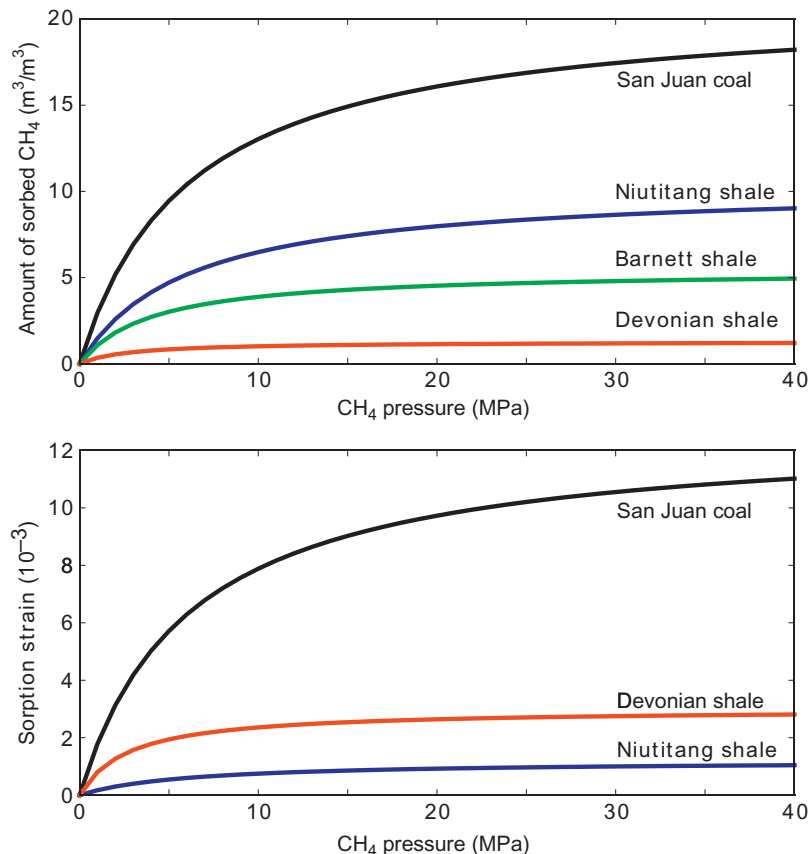


FIGURE 17.11 Sorption amounts and induced strains in unjacketed coal and organic-rich shale samples subjected to CH_4 pressure. Higher affinity of CO_2 over CH_4 in organic-rich pores favors CO_2 - CH_4 exchange. Source: Modified from Chen, T., Feng, X.-T., Pan, Z., 2015. Experimental study of swelling of organic rich shale in methane. *Int. J. Coal Geol.* 150, 64–73; and Shovkun, I., Espinoza, D.N., 2017. Coupled fluid flow-geomechanics simulation in stress-sensitive coal and shale reservoirs: impact of desorption-induced stresses, shear failure, and fines migration. *Fuel* 195, 260–272.

Oil: Enhanced Oil Recovery (EOR)

The oil and gas industry has developed technologies for CO_2 injection and enhanced oil recovery (EOR). CO_2 dissolves in crude oil (typically alkanes with less than 13 carbon atoms at reservoir conditions with $P > 10 \text{ MPa}$ and $T > 320 \text{ K}$), lowers the viscosity of the crude oil, “swells” the oil phase, and promotes oil recovery (Blunt et al., 1993; Chung et al., 1988; Lake et al., 2014). A barrel of such incremental oil requires about 0.1 to 0.4 tons of CO_2 to produce (Martin and Taber, 1992).

Prevailing operational and technical challenges include the availability of CO_2 in large quantities and at economical rates, and improving the sweep efficiency. Viscous fingering, geological heterogeneity, and preferential flow along fractures (natural or induced) limit the sweep efficiency. The Cranfield project combines CO_2 -EOR and permanent CO_2 storage (Lu et al., 2013). Typically, water alternating CO_2 schemes are used to overcome these problems (e.g., Lake et al., 2014).

Hydrates – CO₂–CH₄ Exchange

Hydrate formation is a salient characteristic of water–CO₂ interaction at elevated pressure. The phase boundary is PT-dependent, and cuts across the gas–liquid CO₂ transition before supercritical conditions (Fig. 17.1). Hydrate formation is anticipated under PT conditions found offshore and beneath the permafrost.

Methane hydrate is a potential energy source (estimated accumulation: >500–10,000 Gt of carbon worldwide; Collett, 2002; Ruppel and Pohlman, 2008). Methane can be recovered from hydrate-bearing sediments by depressurization, heating, or chemical injection. In particular, the injection of CO₂ into hydrate-bearing sediments triggers the release of CH₄ and the simultaneous entrapment of CO₂ (Ota et al., 2005a; Zhou et al., 2008). Hence, CH₄–CO₂ replacement addresses two critical needs at once: energy source and CO₂ storage.

The extent of CH₄–CO₂ replacement and its efficiency is affected by a number of factors which include pressure and temperature, specific surface area of the hydrate phase, fluid expansion after replacement, and associated changes in effective stress (Jung et al., 2010). Experimental results show that the CH₄–CO₂ replacement rate increases with rising CO₂ gas pressure until the CO₂ liquefies, and remains constant thereafter (McGrail et al., 2007; Ota et al., 2005b). The replacement ratio increases when a mixture of CO₂ and N₂ is used for CH₄ exchange because the small N₂ molecules boost occupancy and replacement (Park et al., 2006). CH₄–CO₂ replacement occurs locally and advances gradually, so that the overall hydrate mass remains solid (Jung and Santamarina, 2010), and there are no significant changes in the global stiffness of hydrate-bearing sediments during replacement (Espinoza and Santamarina, 2011).

STORAGE EFFICIENCY

The CO₂ saturation and storage efficiency increases in geologic traps where thick CO₂ columns accumulate: buoyancy determines the overpressure, i.e. the capillary pressure difference between CO₂ and water $P_c = P_{CO_2} - P_w$. Then, the CO₂ saturation is estimated from the drainage “capillary pressure versus water saturation” curve of the storage horizon.

The storage efficiency E in reservoirs with subhorizontal caprocks can be very low, in part due to injection fingering, spatial variability of rock properties and ensuing bypassed rock volumes (note: storage efficiency is the volumetric ratio of pore space occupied by CO₂ compared to the available pore space). Typical expected efficiencies are $E < 0.05$ (NETL, 2010; Okwen et al., 2010).

Storage efficiency has important implications on reservoir size. The CO₂ storage capacity G_{CO_2} (Gton) of a reservoir is a function of its areal extent A_t (km²), the mean plume thickness H_{CO_2} (determined by the capillarity so that $H_{CO_2} \leq H_R$ where H_R is the thickness of the reservoir layer), porosity φ , and CO₂ density ρ_{CO_2} (kg/m³)

$$G_{CO_2} = E \cdot \varphi \cdot A_t \cdot H_{CO_2} \cdot \rho_{CO_2} \quad (17.8)$$

Considering a worldwide sequestration target of $G_{CO_2} = 750$ Gt CO₂ over the next 50 years (15 Gt CO₂/year; Espinoza et al., 2011) and supercritical storage conditions (density $\rho_{CO_2} = 600$ kg/m³) in typical reservoirs (column height $H_{CO_2} = 10$ m, porosity $\varphi = 0.2$, high storage efficiency factor $E = 0.055$), the estimated storage area will be $\sim 1,000,000$ km², which is similar to the land-surface area of Texas or France.

Engineered Injection

We may be able to engineer CO_2 injection to attain a higher sweep efficiency. Possible options include: increasing CO_2 viscosity, sequential fluid injection, bio-clogging, and decreasing the capillary factor, $\sigma_{fl} \cdot \cos\theta$, as will be illustrated below.

Experiments with long-chain nonionic surfactants with hydrophilic heads and CO_2 -philic tails show that the CO_2 -water interfacial tension falls from $\sigma_{fl} \sim 50 \text{ mN/m}$ to $\sigma_{fl} \sim 4 \text{ mN/m}$ at a pressure of $P \geq 7 \text{ MPa}$ (Kim and Santamarina, 2014b). The contact angle formed by a water-surfactant droplet resting on a quartz substrate and surrounded by CO_2 increases from $\theta \sim 20^\circ$ at $P = 0.1 \text{ MPa}$ to $\theta \sim 70^\circ$ at $P = 10 \text{ MPa}$. Lower interfacial tension σ_{fl} and a higher contact angle θ combine to produce a marked decrease in the capillary factor $\sigma_{fl} \cdot \cos\theta$. Experimental CO_2 injection tests in pore micro-models and complementary network model simulations demonstrate that the sweep efficiency of CO_2 invasion can be effectively enhanced by lowering the capillary factor $\sigma_{fl} \cdot \cos\theta$ (Fig. 17.12). In particular, the sweep efficiency may be doubled by the addition of surfactants (Kim and Santamarina, 2014b).

MONITORING

The coupled hydro-thermo-chemo-mechanical processes described above and ensuing emergent phenomena demand careful monitoring during injection as well as in the long term.

Monitoring methods take advantage of the differences between physical properties (mass density, bulk stiffness, electrical resistivity and dielectric permittivity), the detection of byproducts from chemical reactions or the consequences of coupled process (from temperature to upheaval-subsidence and microseismicity). Salient observations follow.

Pressure and Temperature

Pressure and temperature monitoring above and within the injection horizon provides valuable insights into the reservoir response to CO_2 injection, and the evolution of the CO_2 plume (e.g., Hovorka et al., 2013). Underlying phenomena that produce a pressure or temperature response include:

- Pressure: fracture and shutoff, poroelastic effects, thermal changes, mid-term CO_2 redistribution, dissolution in host materials, and structural changes associated with salt precipitation, dissolution, and swelling.
- Temperature: depressurization cooling as the injected CO_2 invades the formation away from the injection well (Joule–Thomson effect; Han et al., 2010), depressurization near leak points, and phase transitions (liquid–gas, hydrated formation/dissociation, and CO_2 – CH_4 replacement).

Elastic Waves

The bulk modulus K_{mix} of the sediment can be estimated from the Biot–Gassman equation (Espinoza et al., 2011):

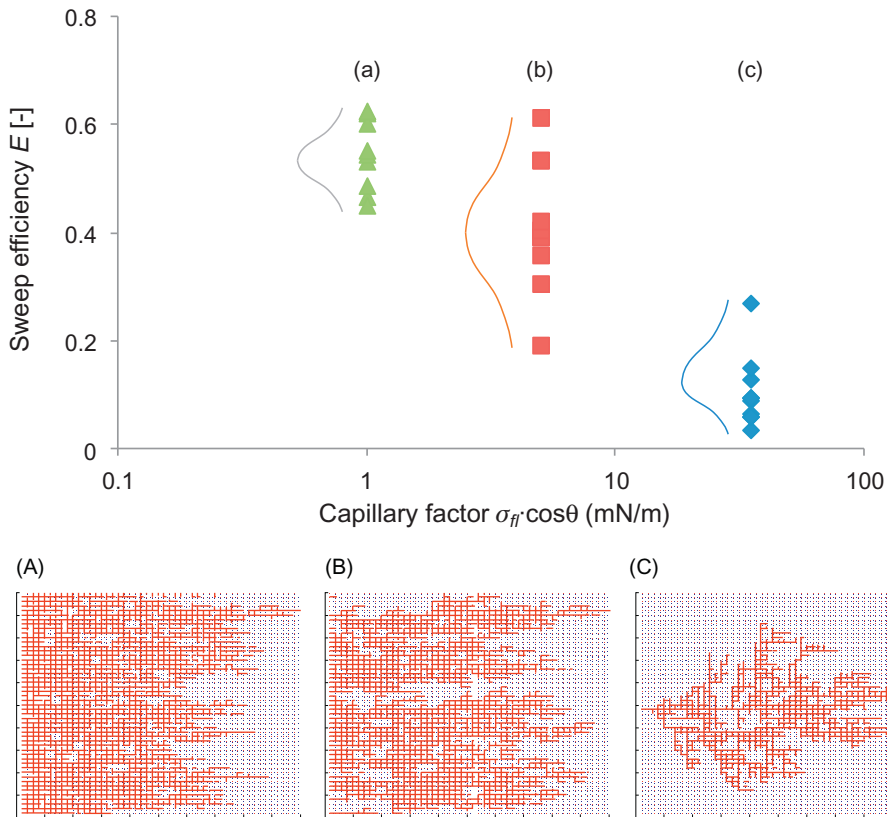


FIGURE 17.12 Pore-network simulations of engineered CO₂ injection: CO₂ invasion pattern and sweep efficiency for different capillary factors $\sigma_{fi} \cdot \cos\theta$. There are 10 network realizations for each capillary factor. Note: 50 × 50 pore network model, initial pressure difference between the inlet and the outlet is $\Delta P_{tot} = 200$ kPa, and constant flow rate is imposed $q_{tot} = 2.8$ mm³/s. Note: simulations highlight the interplay between governing processes and can be readily upscaled. Spatial variability and the geo-plumbing of natural reservoirs exacerbate low sweep efficiencies. *Source: Modified from Kim, S., Santamarina, J.C., 2014b. Engineered CO₂ injection: the use of surfactants for enhanced sweep efficiency. Int. J. Greenh. Gas Control 20, 324–332.*

$$K_{mix} = K_{sk} + \left(1 - \frac{K_{sk}}{K_g}\right)^2 \left[\varphi \left(\frac{S_w}{K_w} + \frac{S_{CO_2}}{K_{CO_2}} \right) + \frac{1-\varphi}{K_g} - \frac{K_{sk}}{K_g^2} \right]^{-1} \quad (17.9)$$

where the subindices represent the mineral skeleton, *sk*, the minerals that make the grains, *g*, the brine, *w*, and the CO₂. The density of the mixture is $\rho_{mix} = (1 - \varphi)\rho_s + \varphi(S_{CO_2}\rho_{CO_2} + S_w\rho_w)$. The compressional V_P and shear V_S wave velocities follow:

$$V_P = \sqrt{\left(\frac{K_{mix} + 4/3 \cdot G_{sk}}{\rho_{mix}} \right)} \quad (17.10)$$

$$V_s = \sqrt{\frac{G_{sk}}{\rho_{mix}}} \quad (17.11)$$

where G_{sk} is the shear modulus of the mineral skeleton. The two most important effects of CO₂ injection on elastic wave propagation include:

- Shear: G_{sk} is more sensitive than K_{mix} to changes in effective stress associated with CO₂ injection and overpressure, and to changes in stiffness due to dissolution (Mavko et al., 2009).
- Bulk: the bulk stiffness of CO₂ is an order of magnitude lower than that of water: $K_{CO_2} \approx 0.1 K_w$ (Span and Wagner, 1996). Therefore, V_p decreases as CO₂ saturation S_{CO_2} increases.

Electrical Resistivity Methods

Electrical conduction in a geological formation involves the movement of hydrated ions in the pore fluid and in adsorbed layers. Surface conduction can be disregarded when the pore fluid has a high ionic strength or when the porous medium has low internal surface area (note: this is the case in potential CO₂ reservoirs, i.e., coarse-grained siliciclastics). Then, the electrical conductivity of the CO₂ reservoir σ_{res} is the volume fraction of the brine $\varphi(1 - S_{CO_2})$ times its conductivity σ_B . Generalizing Archie's law (Santamarina et al., 2001; Guéguen and Palciauskas, 1994):

$$\sigma_{res} = [\varphi^\alpha (1 - S_{CO_2})^\beta] \sigma_B \quad (17.12)$$

where φ is porosity, and α and β are fitting parameters. Clearly, σ_{res} decreases as the CO₂ saturation S_{CO_2} increases.

Microseismicity

Changes in the effective stress or reservoir temperature accompanying CO₂ injection can trigger the sudden release of elastic strain energy (Elsworth et al., 2016). The magnitude of such seismic events is proportional to the shear slip area. The stored strain energy is proportional to rock stiffness, and the seismic characteristics of the geological formations (Bauer et al., 2016; McGarr, 2014). Although microseismic events are difficult to interpret, passive emissions contribute valuable information within a comprehensive injection monitoring strategy.

Surface Heave

Initially, the reservoir expansion caused by small injection volumes has only a local effect. However, as CO₂ injection continues, the surface heave begins to track the reservoir heave once the lateral extent of the reservoir L_{res} exceeds two to four times the burial depth z_{res} . There are two components of reservoir heave (the following analysis applies to $L_{res}/z_{res} > 4$ —see alternative analyses and simulation in Kim and Hosseini, 2015; data in Verdon et al., 2013. Refer to Fig. 17.4 for schematic illustration of long-term CO₂ pressure):

- *Reservoir expansion.* Buoyant CO₂ within the reservoir horizon increases the fluid pressure, decreases the vertical effective stress σ_z' and the formation expands. The stress drop ranges

from $\Delta\sigma_z' = (\gamma_B - \gamma_{CO_2}) \cdot H_{CO_2}$ at the top of the plume to $\Delta\sigma_z' = (\gamma_B - \gamma_{CO_2}) \cdot \varphi \cdot H_{CO_2}$ at the bottom of the plume, where H_{CO_2} is the plume height. Then, the surface heave due to the expansion of the reservoir δ_z^{res} is the integral of the vertical strain,

$$\delta_z^{res} = \int_0^{H_{CO_2}} \varepsilon_z dz = \frac{(\gamma_B - \gamma_{CO_2})(\varphi + 1)}{M_{sk}} \frac{H_{CO_2}^2}{2} \approx 0.03g \frac{H_{CO_2}^2}{V_{sr}^2} \quad (17.13)$$

- The estimate on the right assumes linear elasticity to express the drained constrained modulus M_{sk} —vertical stiffness under zero lateral—in terms of the reservoir shear wave velocity V_{sr} extracted from geophysical surveys (note: g = gravity).
- Unloading and expansion of lower layers.* The Boussinesq elastic solution for a circular reservoir predicts that the heave of layers below the reservoir horizon will be proportional to the reservoir diameter L_{res} , the effective stress change at the bottom of the plume $\Delta\sigma_z' = (\gamma_B - \gamma_{CO_2}) \cdot \varphi \cdot H_{CO_2}$, and inversely proportional to the mean stiffness of the underlying formation E_b . Then,

$$\delta_z^{below} = \frac{\Delta\sigma_z' L_{res}}{E_b} (1 - \nu^2) = \frac{(\gamma_B - \gamma_{CO_2}) \varphi H_{CO_2} L_{res}}{E_b} (1 - \nu^2) \approx 0.02g \frac{H_{CO_2} L_{res}}{V_{sb}^2} \quad (17.14)$$

Analogous to the previous equation, the estimate on the right permits the evaluation of heave from shear wave velocity data in subjacent layers V_{sb} . The areal extent L_{res} in mature reservoirs is much greater than the CO₂ plume thickness H_{CO_2} ; then, Eqs. 17.13 and 17.14 predict that the heave of layers beneath the reservoir will determine the surface response, and the surface heave will continue to increase as the areal extent increases even if the plume height remains constant. For example, consider a reservoir with lateral extent $L_{res} = 4000$ m, plume thickness $H_{CO_2} = 10$ m, $V_{sr} = 1500$ m/s, and $V_{sb} = 2000$ m/s; the anticipated reservoir heave is $\delta_z^{res} = 0.01$ mm, while the heave caused by subjacent layers is $\delta_z^{below} = 1.9$ mm). Heave estimates help select measurement systems, such as GPS, EDM, and/or InSAR. A properly engineered surface monitoring system provides valuable information to track the evolution of the reservoir (Feigl and Thurber, 2009; Newman et al., 2006).

LEAK SEALING

The spatial heterogeneity of the caprock defines paths of least resistance for CO₂ leaks (Cavanagh and Haszeldine, 2014; Meckel et al., 2015). Conductive fractures and abandoned wellbores are preferential paths for CO₂ leakage (Cartwright and Santamarina, 2015; Chioldini et al., 1995).

Several strategies have been proposed to address the risk of CO₂ leakage (Réveillère et al., 2012): (1) control the CO₂ overpressure; (2) enhance CO₂ immobilization in the form of dissolution or capillary trapping; (3) form a hydraulic barrier beneath the overlying layer; and (4) modify the hydraulic properties of the fractures. Approaches to control the latter have considered microbial clogging (Bryant and Britton, 2008; Cunningham et al., 2009), the injection of polymer gels (Sydansk et al., 2005), or suspensions of submicron clay particles to fill cracks (Kim and Santamarina, 2013). A pronounced decrease in leakage rates was attained as fractured

shale specimens were subjected to successive sealing treatments; for example, shales with hair-line cracks experienced an increase in the breakthrough pressure from ~ 30 kPa before treatment to more than $P \sim 1$ MPa after the injection of clay slurries (Kim and Santamarina, 2013).

CLOSING COMMENTS: THE RANGE OF DIFFERENT PROCESSES

This chapter identified concurrent hydro-chemo-thermo-mechanical processes that affect the short- and long-term response of geological CO_2 storage sites. We explored mixed-fluid phenomena, reactive fluid-formation interaction, and associated changes in permeability and effective stresses.

Coupled processes affect all forms of CO_2 geological storage, from stratigraphic trapping to chemo-physical interactions in coal, shale, EOR, and CH_4-CO_2 exchange in hydrates. Simple scaling relationships facilitate first-order spatial and temporal analyses of coupled processes in CO_2 geological storage. Table 17.1 summarizes important dimensionless ratios for processes described in this chapter (see related analyses and implications in Kim and Santamarina, 2014a, b; Espinoza and Santamarina, 2017).

TABLE 17.1 Governing Dimensionless Ratios for Geologic Carbon Storage (Kim and Santamarina, 2014a; Espinoza and Santamarina, 2017; Kim and Santamarina, 2014b)

Dimensionless ratio	Expression	Physical interpretation
Mobility number M	$M = \frac{\mu_{\text{CO}_2}}{\mu_w}$	Ratio between CO_2 and water viscosities. Susceptibility to viscous fingering
Capillary number C	$C = \frac{q\mu_{\text{CO}_2}}{\sigma_f \cos\theta}$	Ratio between viscous and capillary forces
Rayleigh number Ra	$Ra = \frac{k\Delta\gamma H_{\text{CO}_2}}{\mu\varphi D}$	Ratio between convection rate and diffusion rate. Susceptibility to convective instability
Bond number B	$B = \frac{\Delta\gamma k}{\sigma_f \cos\theta}$	Ratio between conditions for gravity-driven CO_2 advective flow and capillary trapping
Sealing number SI (also: trapping number for reservoir)	$SI = \frac{4\sigma_f \cos\theta}{d_{ch} H_{\text{CO}_2} \Delta\gamma}$	Ratio between capillary breakthrough pressure and buoyant CO_2 overpressure
Stability number St	$St = \frac{\sigma'_z}{H_{\text{CO}_2} \Delta\gamma}$	Ratio between initial vertical effective stress at depth z and overpressure
Damköhler number	$Da = \frac{\kappa L_{ch}}{v_{ave}}$	Ratio between advection time and time for chemical reactions
Peclet number	$Pe = \frac{v_{ave} L_{ch}}{D}$	Ratio between diffusion and advection times

Note: μ_{CO_2} , CO_2 viscosity; μ_w , water viscosity; q , flow rate; σ_f , interfacial tension; θ , contact angle; γ_i , unit weight; $\Delta\gamma$, $\gamma_B - \gamma_{\text{CO}_2}$; k , permeability; φ , porosity; D , coefficient of molecular diffusion; H_{CO_2} , CO_2 pool thickness; d_{ch} , characteristic pore size; σ'_z , vertical effective stress; κ , kinetic rate of chemical reaction; L_{ch} , characteristic length; v_{ave} , average flow velocity.

These dimensionless ratios help to identify regimes and controlling processes that require further analysis before diving into complex simulations that involve a large number of constitutive equations and parameters. This approach leads to more robust analyses and the design of more efficient monitoring strategies.

Coupled processes and ensuing emergent phenomena demand careful monitoring and data analysis during injection and long-term storage, as measured parameters are inherently affected by all concurrent processes.

Acknowledgments

Support for this research was provided by the US Department of Energy. G. Abelskamp edited the manuscript. We are grateful to the anonymous reviewers for detailed comments and valuable insights.

References

- Alonso, E.E., Gens, A., Josa, A., 1990. A constitutive model for partially saturated soils. *Geotechnique* 40, pp. 405–430.
- Azaroual, M., Pruess, K., Fouillac, C., 2007. Feasibility of using supercritical CO₂ as heat transmission fluid in the EGS (Enhanced Geothermal Systems) integrating the carbon storage constraints. In: ENGINE – Enhanced Geothermal Innovative Network for Europe Workshop 2: Exploring High Temperature Reservoirs: New Challenges for Geothermal Energy. Volterra, Italy.
- Bauer, R.A., Carney, M., Finley, R.J., 2016. Overview of microseismic response to CO₂ injection into the Mt. Simon saline reservoir at the Illinois Basin-Decatur Project. *Int. J. Greenh. Gas Control* 54, pp. 378–388.
- Bielinski, A., 2007. Numerical Simulation of CO₂ Sequestration in Geological Formations. Universitat Stuttgart, Stuttgart, 117 p.
- Blunt, M., Fayers, F.J., Orr, F.M., 1993. Carbon-dioxide in enhanced oil-recovery. *Energy Convers. Manage.* 34, pp. 1197–1204.
- Bryant, S., Britton, L., 2008. Mechanistic Understanding of Microbial Plugging for Improved Sweep Efficiency. US DOE NETL Report DE-FC26-04NT15524.
- Busch, A., Alles, S., Gensterblum, Y., Prinz, D., Dewhurst, D.N., Raven, M.D., et al., 2008. Carbon dioxide storage potential of shales. *Int. J. Greenh. Gas Control* 2, pp. 297–308.
- Carman, P.C., 1956. Flow of Gases Through Porous Media. Butterworths Scientific Publications, London, UK.
- Cartwright, J., Santamarina, C., 2015. Seismic characteristics of fluid escape pipes in sedimentary basins: implications for pipe genesis. *Mar. Pet. Geol.* 65, pp. 126–140.
- Cartwright, J., James, D., Bolton, A., 2003. The genesis of polygonal fault systems: a review. *Geol. Soc. Lond. Spec. Publ.* 216, pp. 223–243.
- Cavanagh, A.J., Haszeldine, R.S., 2014. The Sleipner storage site: capillary flow modeling of a layered CO₂ plume requires fractured shale barriers within the Utsira Formation. *Int. J. Greenh. Gas Control* 21, pp. 101–112.
- Ceglarska-Stefanska, G., Zarebska, K., 2002. The competitive sorption of CO₂ and CH₄ with regard to the release of methane from coal. *Fuel Process. Technol.* 77, pp. 423–429.
- Cha, M., 2012. Mineral Dissolution in Sediments. Georgia Institute of Technology, Atlanta, USA, 152 p.
- Cha, M., Santamarina, J.C., 2014. Dissolution of randomly distributed soluble grains: post-dissolution k₀-loading and shear. *Géotechnique* 64, pp. 828–836.
- Chalbaud, C., Robin, M., Lombard, J.M., Martin, F., Egermann, P., Bertin, H., 2009. Interfacial tension measurements and wettability evaluation for geological CO₂ storage. *Adv. Water Resour.* 32, pp. 98–109.
- Chen, T., Feng, X.-T., Pan, Z., 2015. Experimental study of swelling of organic rich shale in methane. *Int. J. Coal Geol.* 150, pp. 64–73.
- Chi, S.M., Morsi, B.I., Klinzing, G.E., Chiang, S.H., 1988. Study of interfacial properties in the liquid carbon dioxide-water-coal system. *Energy Fuels* 2, pp. 141–145.
- Chiodini, G., Frondini, F., Ponziani, F., 1995. Deep structures and carbon dioxide degassing in Central Italy. *Geothermics* 24, pp. 81–94.

- Chung, F.T., Jones, R.A., Nguyen, H.T., 1988. Measurements and correlations of the physical properties of CO₂-heavy crude oil mixtures. *SPE Reserv. Eng.* 3, pp. 822–828.
- Collett, T.S., 2002. Energy resource potential of natural gas hydrates. *AAPG Bull.* 86, pp. 1971–1992.
- Cunningham, A.B., Gerlach, R., Spangler, L., Mitchell, A.C., 2009. Microbially enhanced geologic containment of sequestered supercritical CO₂. *Energy Procedia* 1, pp. 3245–3252.
- De Paola, N., Faulkner, D., Collettini, C., 2009. Brittle versus ductile deformation as the main control on the transport properties of low-porosity anhydrite rocks. *J. Geophys. Res. Solid Earth* 114, B06211, pp. 1–17.
- Dooley, J.J., Dahowski, R.T., Davidson, C.L., Wise, M.A., Gupta, N., Kim, S.H., et al., 2006. Carbon dioxide capture and geologic storage: a core element of a global energy technology strategy to address climate change. In: A Technology Report from the Second Phase of the Global Energy Technology Strategy Program. Joint Global Change Research Institute (JGCRI), Battelle Memorial Institute, College Park, MD, USA.
- Downey, M.W., 1984. Evaluating seals for hydrocarbon accumulations. *AAPG Bull.* 68, pp. 1752–1763.
- Elsworth, D., Spiers, C.J., Niemeijer, A.R., 2016. Understanding induced seismicity. *Science* 354, pp. 1380–1381.
- Espinoza, D.N., Santamarina, J.C., 2010. Water-CO₂-mineral systems: interfacial tension, contact angle, and diffusion—implications to CO₂ geological storage. *Water Resour. Res.* 46, W07537, pp. 1–10.
- Espinoza, D.N., Santamarina, J.C., 2011. P-wave monitoring of hydrate-bearing sand during CH₄-CO₂ replacement. *Int. J. Greenh. Gas Control* 5 (4), pp. 1031–1038.
- Espinoza, D.N., Santamarina, J.C., 2012. Clay interaction with liquid and supercritical CO₂: the relevance of electrical and capillary forces. *Int. J. Greenh. Gas Control* 10, pp. 351–362.
- Espinoza, D.N., Santamarina, J.C., 2017. CO₂ breakthrough—caprock sealing efficiency and integrity for carbon geological storage. *Int. J. Greenh. Gas Control* 66, pp. 218–229.
- Espinoza, D.N., Kim, S., Santamarina, J.C., 2011. CO₂ geological storage—geotechnical implications. *KSCE J. Civil Eng.* 15, pp. 707–719.
- Espinoza, D., Pereira, J.-M., Vandamme, M., Dangla, P., Vidal-Gilbert, S., 2015. Desorption-induced shear failure of coal bed seams during gas depletion. *Int. J. Coal Geol.* 137, pp. 142–151.
- Espinoza, D.N., Shovkun, I., Makni, O., Lenoir, N., 2016. Natural and induced fractures in coal cores imaged through X-ray computed microtomography—impact on desorption time. *Int. J. Coal Geol.* 154, pp. 165–175.
- Feigl, K.L., Thurber, C.H., 2009. A method for modelling radar interferograms without phase unwrapping: application to the M5 FawnSkin, California earthquake of 1992 December 4. *Geophys. J. Int.* 176, pp. 491–504.
- Fenghour, A., Wakeham, W.A., Vesovic, V., 1998. The viscosity of carbon dioxide. *J. Phys. Chem. Ref. Data* 27, pp. 31–44.
- Fleury, M., Pironon, J., Nindre, L., Bildstein, O., Berne, P., Lagneau, V., et al., 2010. Evaluating sealing efficiency of caprocks for CO₂ storage: an overview of the Geocarbone Integrity program and results. *Oil Gas Sci. Technol.* 65, pp. 435–444.
- Fredd, C.N., Fogler, H.S., 1998a. The kinetics of calcite dissolution in acetic acid solutions. *Chem. Eng. Sci.* 53, pp. 3863–3874.
- Fredd, C.N., Fogler, H.S., 1998b. Influence of transport and reaction on wormhole formation in porous media. *AIChE J.* 44, pp. 1933–1949.
- Funazukuri, T., Ishiwata, Y., Wakao, N., 1992. Predictive correlation for binary diffusion-coefficients in dense carbon-dioxide. *AIChE J.* 38, pp. 1761–1768.
- Gherardi, F., Xu, T., Pruess, K., 2007. Numerical modeling of self-limiting and self-enhancing caprock alteration induced by CO₂ storage in a depleted gas reservoir. *Chem. Geol.* 244, pp. 103–129.
- Golfier, F., Zarcone, C., Bazin, B., Lenormand, R., Lasseux, D., Quintard, M., 2002. On the ability of a Darcy-scale model to capture wormhole formation during the dissolution of a porous medium. *J. Fluid Mech.* 457, pp. 213–254.
- Guéguen, Y., Palcuskas, V., 1994. Introduction to the Physics of Rocks. Princeton University Press, Princeton, NJ, USA, 294 p.
- Guiltinan, E.J., Cardenas, M.B., Bennett, P.C., Zhang, T., Espinoza, D.N., 2017. The effect of organic matter and thermal maturity on the wettability of supercritical CO₂ on organic shales. *Int. J. Greenh. Gas Control* 65, pp. 15–22.
- Gunter, W.D., Perkins, E.H., Hutcheon, I., 2000. Aquifer disposal of acid gases: modelling of water-rock reactions for trapping of acid wastes. *Appl. Geochem.* 15, pp. 1085–1095.
- Han, W.S., McPherson, B.J., Lichtner, P.C., Wang, F.P., 2010. Evaluation of trapping mechanisms in geologic CO₂ sequestration: case study of SACROC northern platform, a 35-year CO₂ injection site. *Am. J. Sci.* 310, pp. 282–324.

- Hassanzadeh, H., Pooladi-Darvish, M., Keith, D.W., 2007. Scaling behavior of convective mixing, with application to geological storage of CO₂. *AIChE J.* 53, pp. 1121–1131.
- Hesse, M., Tchelepi, H., Orr, F., 2006. Scaling analysis of the migration of CO₂ in saline aquifers. In: SPE Annual Technical Conference and Exhibition, San Antonio, TX, USA. SPE 102796.
- Hovorka, S.D., Meckel, T.A., Treviño, R.H., 2013. Monitoring a large-volume injection at Cranfield, Mississippi—project design and recommendations. *Int. J. Greenh. Gas Control* 18, pp. 345–360.
- IPCC, 2005. IPCC special report on carbon dioxide capture and storage. In: Metz, B., Davidson, O., de Coninck, H.C., Loos, M., Meyer, L.A. (eds.), Prepared by Working Group III of the Intergovernmental Panel on Climate Change. Cambridge University Press, Cambridge, UK, p. 442.
- Jaccard, M.K., 2005. Sustainable Fossil Fuels: The Unusual Suspect in the Quest for Clean and Enduring Energy. Cambridge University Press, Cambridge.
- Jung, J., Santamarina, J.C., 2010. CH₄-CO₂ replacement in hydrate-bearing sediments: a pore-scale study. *Geochem. Geophys. Geosyst.* 11, Q0AA13, pp. 1–8.
- Jung, J.-W., Wan, J., 2012. Supercritical CO₂ and ionic strength effects on wettability of silica surfaces: equilibrium contact angle measurements. *Energy Fuels* 26, pp. 6053–6059.
- Jung, J., Espinoza, D.N., Santamarina, J.C., 2010. Properties and phenomena relevant to CH₄-CO₂ replacement in hydrate-bearing sediments. *J. Geophys. Res. Solid Earth* 115, B10102, pp. 1–16.
- Kang, S.M., Fathi, E., Ambrose, R.J., Akkutlu, I.Y., Sigal, R.F., 2011. Carbon dioxide storage capacity of organic-rich shales. *SPE J.* 16, pp. 842–855.
- Kim, S., 2012. CO₂ Geological Storage: Hydro-Chemo-Mechanically Coupled Phenomena and Engineered Injection. (PhD Dissertation). Georgia Institute of Technology, Atlanta, GA, USA, 188 p.
- Kim, S., Hosseini, S., 2015. Hydro-thermo-mechanical analysis during injection of cold fluid into a geologic formation. *Int. J. Rock Mech. Min. Sci.* 77, pp. 220–236.
- Kim, S., Santamarina, J.C., 2013. CO₂ breakthrough and leak-sealing – experiments on shale and cement. *Int. J. Greenh. Gas Control* 19, pp. 471–477.
- Kim, S., Santamarina, J.C., 2014a. CO₂ geological storage: hydro-chemo-mechanical analyses and implications. *Greenh. Gas. Sci. Technol.* 4, pp. 528–543.
- Kim, S., Santamarina, J.C., 2014b. Engineered CO₂ injection: the use of surfactants for enhanced sweep efficiency. *Int. J. Greenh. Gas Control* 20, pp. 324–332.
- Kim, S., Santamarina, J.C., 2015. Reactive fluid flow in CO₂ storage reservoirs: a 2-D pore network model study. *Greenh. Gas. Sci. Technol.* 5, pp. 462–473.
- Lake, L.W., Johns, R.T., Rossen, W.R., Pope, G.A., 2014. Fundamentals of Enhanced Oil Recovery. Society of Petroleum Engineers, 496 p.
- Liong, K.K., Wells, P.A., Foster, N.R., 1992. Diffusion of fatty-acid esters in supercritical carbon-dioxide. *Ind. Eng. Chem. Res.* 31, pp. 390–399.
- Lu, J., Kordi, M., Hovorka, S., Meckel, T., Christopher, C., 2013. Reservoir characterization and complications for trapping mechanisms at Cranfield CO₂ injection site. *Int. J. Greenh. Gas Control* 18, pp. 361–374. Available from: <https://doi.org/10.1016/j.ijggc.2012.10.007>.
- Lyklema, J., 1995. Fundamentals of Interface and Colloid Science. Volume II: Solid–Liquid Interfaces. Academic Press, New York.
- Martin, D.F., Taber, J., 1992. Carbon dioxide flooding. *J. Pet. Technol.* 44, pp. 396–400.
- Mavko, G., Mukerji, T., Dvorkin, J., 2009. The Rock Physics Handbook, Tools for Seismic Analysis of Porous Media, second edition. Cambridge University Press, New York, 512 p.
- McGarr, A., 2014. Maximum magnitude earthquakes induced by fluid injection. *J. Geophys. Res. Solid Earth* 119, pp. 1008–1019.
- McGrail, B.P., Schaeff, H.T., White, M.D., Zhu, T., Kulkarni, A.S., Hunter, R.B., et al., 2007. Using Carbon Dioxide to Enhance Recovery of Methane From Gas Hydrate Reservoirs: Final Summary Report. Pacific Northwest National Laboratory (PNNL), Richland, WA, USA.
- Meckel, T., Bryant, S., Ganesh, P.R., 2015. Characterization and prediction of CO₂ saturation resulting from modeling buoyant fluid migration in 2D heterogeneous geologic fabrics. *Int. J. Greenh. Gas Control* 34, pp. 85–96.
- Miri, R., Hellevang, H., 2016. Salt precipitation during CO₂ storage—a review. *Int. J. Greenh. Gas Control* 51, pp. 136–147.

- Mohamed, I., Nasr-El-Din, H., 2012. Formation damage due to CO₂ sequestration in deep saline carbonate aquifers. In: SPE International Symposium and Exhibition on Formation Damage Control. Society of Petroleum Engineers, Lafayette, Louisiana, USA. SPE-151142-MS.
- Netl, M., 2010. Carbon Sequestration Atlas of the United States and Canada. US Department of Energy, Office of Fossil Energy, National Energy Technology Laboratory.
- Newman, A.V., Dixon, T.H., Gourmelen, N., 2006. A four-dimensional viscoelastic deformation model for Long Valley Caldera, California, between 1995 and 2000. *J. Volcanol. Geother. Res.* 150, pp. 244–269.
- Okwen, R.T., Stewart, M.T., Cunningham, J.A., 2010. Analytical solution for estimating storage efficiency of geologic sequestration of CO₂. *Int. J. Greenh. Gas Control* 4, pp. 102–107.
- Ota, M., Morohashi, K., Abe, Y., Watanabe, M., Smith Jr., R.L., Inomata, H., 2005a. Replacement of CH₄ in the hydrate by use of liquid CO₂. *Energy Convers. Manage.* 46, pp. 1680–1691.
- Ota, M., Abe, Y., Watanabe, M., Smith, R.L., Inomata, H., 2005b. Methane recovery from methane hydrate using pressurized CO₂. *Fluid Phase Equil.* 228, pp. 553–559.
- Palmer, I., Mansoori, J., 1996. How permeability depends on stress and pore pressure in coalbeds: a new model. In: SPE Annual Technical Conference and Exhibition. Society of Petroleum Engineers.
- Pan, Z., Connell, L.D., 2012. Modelling permeability for coal reservoirs: a review of analytical models and testing data. *Int. J. Coal Geol.* 92, pp. 1–44.
- Park, Y., Kim, D.-Y., Lee, J.-W., Huh, D.-G., Park, K.-P., Lee, J., et al., 2006. Sequestering carbon dioxide into complex structures of naturally occurring gas hydrates. *Proc. Natl. Acad. Sci. U.S.A.* 103, pp. 12690–12694.
- Peng, D.Y., Robinson, D.B., 1976. A new two-constant equation of state. *Ind. Eng. Chem. Fundamentals* 15, pp. 59–64.
- Peysson, Y., Andre, L., Azaroual, M., 2014. Well injectivity during CO₂ storage operations in deep saline aquifers—part 1: experimental investigation of drying effects, salt precipitation and capillary forces. *Int. J. Greenh. Gas Control* 22, pp. 291–300.
- Phadnis, H.S., Santamarina, J.C., 2011. Bacteria in sediments: pore size effects. *Geotech. Lett.* 1, pp. 91–93.
- Phillips, O.M., 2009. Geological Fluid Dynamics: Sub-Surface Flow and Reactions. Cambridge University Press, Cambridge, 285 p.
- Pokrovsky, O.S., Golubev, S.V., Schott, J., 2005. Dissolution kinetics of calcite, dolomite and magnesite at 25 °C and 0 to 50 atm pCO₂. *Chem. Geol.* 217, pp. 239–255.
- Pruess, K., 2011. ECO2M: A TOUGH2 Fluid Property Module for Mixtures of Water, NaCl, and CO₂, Including Super- and Sub-Critical Conditions, and Phase Change Between Liquid and Gaseous CO₂. Lawrence Berkeley National Laboratory, Berkeley, CA, USA.
- Ren, X.W., Santamarina, J.C., 2018. The hydraulic conductivity of sediments: a pore size perspective. *J. Eng. Geol.* 233, pp. 48–54.
- Réveillère, A., Rohmer, J., Manceau, J.C., 2012. Hydraulic barrier design and applicability for managing the risk of CO₂ leakage from deep saline aquifers. *Int. J. Greenh. Gas Control* 9, pp. 62–71.
- Riaz, A., Hesse, M., Tchelepi, H.A., Orr, F.M., 2006. Onset of convection in a gravitationally unstable diffusive boundary layer in porous media. *J. Fluid Mech.* 548, pp. 87–111.
- Rotenberg, Y., Boruvka, L., Neumann, A., 1983. Determination of surface tension and contact angle from the shapes of axisymmetric fluid interfaces. *J. Colloid Interface Sci.* 93, pp. 169–183.
- Ruppel, C., Pohlman, J., 2008. Climate change and the global carbon cycle: perspectives and opportunities. *Fire Ice: Meth. Hydr. Newsl.* 8, pp. 5–8.
- Sánchez, M., Gens, A., Guimaraes, L.N., Olivella, S., 2005. A double structure generalized plasticity model for expansive materials. *Int. J. Num. Anal. Methods Geomech.* 29, pp. 751–787.
- Santamarina, J.C., Klein, K.A., Fam, M.A., 2001. Soils and Waves. Wiley, New York, 488 p.
- Scott, M.A., Mazumder, S., Jiang, J., 2012. Permeability increase in Bowen Basin coal as a result of matrix shrinkage during primary depletion. In: SPE Asia Pacific Oil and Gas Conference and Exhibition. Society of Petroleum Engineers.
- Shin, H., Santamarina, J.C., 2009. Mineral dissolution and the evolution of k₀. *J. Geotech. Geoenvir. Eng.* 135, pp. 1141–1147.
- Shin, H., Santamarina, J., 2011. Desiccation cracks in saturated fine-grained soils: particle-level phenomena and effective-stress analysis. *Géotechnique* 61, pp. 961–972.
- Shin, H., Santamarina, J.C., Cartwright, J.A., 2008. Contraction-driven shear failure in compacting uncemented sediments. *Geology* 36, pp. 931–934.

- Shin, H., Santamarina, J.C., Cartwright, J.A., 2010. Displacement field in contraction-driven faults. *J. Geophys. Res.* 115, B07408, pp. 1–13.
- Shovkun, I., Espinoza, D.N., 2017. Coupled fluid flow-geomechanics simulation in stress-sensitive coal and shale reservoirs: impact of desorption-induced stresses, shear failure, and fines migration. *Fuel* 195, pp. 260–272.
- Sloan, E.D., Koh, C.A., 2007. *Clathrate Hydrates of Natural Gases*, third edition. CRC Press, Boca Raton, FL, 752 p.
- Span, R., Wagner, W., 1996. A new equation of state for carbon dioxide covering the fluid region from the triple point temperature to 1,100 K at pressures up to 800 MPa. *J. Phys. Chem. Ref. Data* 25, pp. 1509–1596.
- Spycher, N., Pruess, K., Ennis-King, J., 2003. CO₂-H₂O mixtures in the geological sequestration of CO₂. I. Assessment and calculation of mutual solubilities from 12 to 100°C and up to 600 bar. *Geochim. Cosmochim. Acta* 67, pp. 3015–3031.
- Stumm, W., 1992. *Chemistry of the Solid-Water Interface: Processes at the Mineral-Water and Particle-Water Interface in Natural Systems*. Wiley, New York, 428 p.
- Stumm, W., Morgan, J.J., 1996. *Aquatic Chemistry: Chemical Equilibria and Rates in Natural Waters*. John Wiley and Sons, New York, 1022 p.
- Sydansk, R.D., Xiong, Y., Al-Dhafeeri, A.M., Schrader, R.J., Seright, R.S., 2005. Characterization of partially formed polymer gels for application to fractured production wells for water-shutoff purposes. *SPE Prod. Facil.* 20, pp. 240–249.
- Takenouchi, S., Kennedy, G., 1965. Dissociation pressures of the phase CO₂·5.75H₂O. *J. Geol.* 73, pp. 383–390.
- Verdon, J.P., Kendall, J.-M., Stork, A.L., Chadwick, R.A., White, D.J., Bissell, R.C., 2013. Comparison of geomechanical deformation induced by megatonne-scale CO₂ storage at Sleipner, Weyburn, and In Salah. *Proc. Natl. Acad. Sci. U.S.A.* 110, pp. E2762–E2771.
- Watson, M.N., Zwingmann, N., Lemon, N.M., 2004. The Ladbroke Grove-Katnook carbon dioxide natural laboratory: a recent CO₂ accumulation in a lithic sandstone reservoir. *Energy* 29, pp. 1457–1466.
- Wellman, T., Grigg, R., McPherson, B., Svec, R., Peter, C., 2003. Evaluation of CO₂-brine-reservoir rock interaction with laboratory flow tests and reactive transport modeling. In: *SPE International Symposium on Oilfield Chemistry*. Houston, TX, USA.
- Wellman, T.P., Shapiro, A.M., Hill, M.C., 2009. Effects of simplifying fracture network representation on inert chemical migration in fracture-controlled aquifers. *Water Resour. Res.* 45, W01416, pp. 1–21.
- Zhou, X.T., Fan, S.S., Liang, D.Q., Du, J.W., 2008. Determination of appropriate condition on replacing methane from hydrate with carbon dioxide. *Energy Convers. Manage.* 49, pp. 2124–2129.